JOURNAL OF THE AMERICAN CHEMICAL SOCIETY

Article

Cite This: *J. Am. Chem. Soc.* 2018, 140, 12001−12009

pubs.acs.org/JACS

Impact of Pressure on Magnetic Order in Jarosite

Ryan A. Klein,[†] James P. S. Walsh,[†] Samantha M. Clarke,[†] Yinsheng Guo,[†] Wenli Bi,[‡,§] Gilberto Fabbris,[‡] Yue Meng,[‡,∥] Daniel Haskel,[‡] E. Ercan Alp,[‡] Richard P. Van Duyne,[†] Steven D. Jacobsen,[⊥] and Danna E. Freedman*,[†]

[†]Department of Chemistry, Northwestern University, Evanston, Illinois 60208, United States
[‡]Advanced Photon Source, Argonne National Laboratory, 9700 South Cass Avenue, Lemont, Illinois 60439, United States
[§]Department of Geology, University of Illinois at Urbana−Champaign, Urbana, Illinois 61801, United States
[∥]HPCAT, Geophysical Laboratory, Carnegie Institute of Washington, Argonne, Illinois 60439, United States
[⊥]Department of Earth and Planetary Sciences, Northwestern University, Evanston, Illinois 60208, United States

Supporting Information

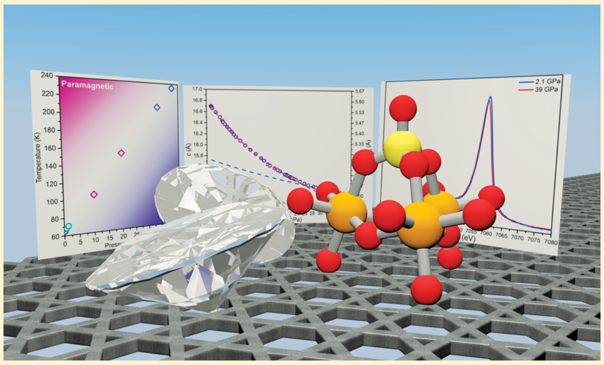

ABSTRACT: Jarosite, a mineral with a kagomé lattice, displays magnetic frustration yet orders magnetically below 65 K. As magnetic frustration can engender exotic physical properties, understanding the complex magnetism of jarosite comprises a multidecade interdisciplinary challenge. Unraveling the nature of the disparate magnetic coupling interactions that lead to magnetic order in jarosite remains an open question. Specifically, there is no observed trend in the interlayer spacing with magnetic order. Similarly, the relationship between metal−ligand bond distance and magnetic order remains uninvestigated. Here, we use applied pressure to smoothly vary jarosite's structure without manipulating the chemical composition, enabling a chemically invariant structure−function study. Using single-crystal and powder X-ray diffraction, we show that high applied pressures alter both the interlayer spacing and the metal−ligand bond distances. By harnessing a suite of magnetic techniques under pressure, including SQUID-based magnetometry, time-resolved synchrotron Mössbauer spectroscopy, and X-ray magnetic circular dichroism, we construct the magnetic phase diagram for jarosite up to 40 GPa. Notably, we demonstrate that the magnetic ordering temperature increases dramatically to 240 K at the highest pressures. Additionally, we conduct X-ray emission spectroscopy, Mössbauer spectroscopy, and UV−visible absorption spectroscopy experiments to comprehensively map the magnetic and electronic structures of jarosite at high pressure. We use these maps to construct chemically pure magnetostructural correlations which fully explain the nature and role of the disparate magnetic coupling interactions in jarosite.

INTRODUCTION

Over the past several decades, researchers across an unusually diverse range of fields, including earth and planetary sciences,[1−4] condensed matter physics,[5−7] and synthetic inorganic chemistry,[8,9] strove to study jarosite, $KFe_3(OH)_6(SO_4)_2$, and to understand its intriguing magnetic properties. Jarosite's perfect 2D kagomé lattice of antiferromagnetically coupled Fe ions causes magnetic frustration.[5,7,10] The geometry of the lattice precludes the simultaneous satisfaction of antiferromagnetic interactions, acting to suppress magnetic order. Despite the structurally perfect kagomé lattice, jarosite orders antiferromagnetically at 65 K due to a Dzyaloshinskii−Moriya (DM) interaction.[11] Yet, the precise roles of the disparate magnetic coupling interactions that lead to magnetic order in jarosite are not fully understood. Therefore, outstanding questions surrounding the mechanism of 3D magnetic order remain, even after numerous magnetic studies on chemical series of jarosite congeners that sought to elucidate the underlying factors that contribute to the relatively high ordering temperature in jarosite.[9−11]

Prior magnetostructural studies of jarosite induced structural changes by modification of the identity of the monocation. Notably, these substitutions varied the interlayer spacing, but the local coordination of the FeO_6 octahedra did not change. These careful chemical substitution studies revealed that three main coupling interactions determine jarosite's magnetic behavior. These interactions are the antiferromagnetic coupling between Fe ions within the kagomé plane, the intralayer ferromagnetic coupling of canted spins, and the interlayer antiferromagnetic coupling of the canted spins. First, pairs of Fe ions couple antiferromagnetically within the kagomé layers. Second, the DM interaction cants the spins in each equilateral triangle of Fe ions out of the *ab* plane.[10]

Received: May 28, 2018
Published: July 31, 2018

DOI: 10.1021/jacs.8b05601
J. Am. Chem. Soc. 2018, 140, 12001−12009

Within a layer, the spins cant out of the *ab* plane in the same direction along the *c*-axis, causing an "umbrella structure" of spins.[5] When the DM interaction correlates the three spin centers in an individual triangle, it creates a so-called triangular spin plaquette, which behaves as its own magnetic moiety in the magnetic structure. Above the Néel temperature, adjacent spin plaquettes couple ferromagnetically to form 2D correlated areas in the kagomé layer, engendering a weak net magnetic moment within each layer. Finally, at the Néel temperature, interlayer coupling of the areas of 2D correlation in each layer engenders the onset of magnetic order in which the layers of plaquettes align antiferromagnetically with each other.

The various contributing coupling interactions that lead to magnetic order are well-defined, but the underlying chemical and structural features within jarosite that engender this complex ordering behavior remain only partially understood. For example, there is no trend observed in the Néel temperature as a function of the interlayer spacing, which is a highly counterintuitive finding. This result contrasts with the magnetic order exhibited by the monocation-substituted V^{3+} family of jarosite congeners.[10,11] In this family of jarosite species, the transition ions couple ferromagnetically within the kagomé lattice. Magnetic order arises from interlayer antiferromagnetic coupling, and the ordering temperature increases monotonically with decreasing interlayer spacing.[18] In both the Fe^{3+} and V^{3+} systems, the local environment around the transition ion remains constant across the substituted series while the interlayer spacing changes with the identity of the cation.[9,10,17,18] Therefore, the interlayer spacing is critical in determining the magnetic ordering temperature in the V^{3+} jarosite family, whereas it apparently does not influence the magnetic ordering temperature in the Fe^{3+} family of jarosite compounds.

To complete a pure magnetostructural study, we sought an experimental parameter that systematically varies the interlayer spacing and FeO_6 octahedra bond metrics without altering jarosite's chemical formula. Therefore, we turned to high applied pressure as a synthetic tool. External pressures represent an extremely useful, albeit underutilized, synthetic tool in inorganic chemistry.[12,13] The application of pressure acts on the magnitude of crystal field splitting, a material's bandgap, and magnetic coupling interactions. As such, pressure can induce structural, electronic, and magnetic phase transitions. For example, high applied pressures can cause spin crossover transitions,[14−16] change conductivity,[17] drastically alter magnetic ordering,[18] or lead to changes in the nature of hydrogen bonding.[19] Despite the utility of hydrostatic pressures for effecting desired changes in materials' electronic and magnetic structures, there is currently no thorough study of the effects of pressure on jarosite's structural, magnetic, and electronic properties.

Herein, we use high pressures to elucidate the mechanism of magnetic order in jarosite. We use pressure to tune the interlayer spacing and the FeO_6 coordination sphere, and we measure the effect on jarosite's magnetoelectronic structure. To that end, we characterize jarosite's structure (powder and single-crystal X-ray diffraction), its vibrational modes (Raman spectroscopy), its magnetic structure (SQUID magnetometry, time-domain synchrotron Mössbauer spectroscopy, X-ray magnetic circular dichroism), and its electronic structure (Mössbauer spectroscopy, X-ray emission spectroscopy, X-ray absorption near edge spectroscopy, UV−visible absorption spectroscopy, optical microscopy) up to 40 gigapascals (GPa) of applied pressure. This panoply of techniques enables us to map the structure, electronic properties, and magnetic phase diagram for jarosite as a function of pressure. By integrating the results from these techniques, we complete the previous efforts to characterize jarosite's magnetic structure. We uniquely elucidate the mechanism for magnetic order in jarosite and definitively show that metal−ligand covalency, and not interlayer spacing, determines the Néel temperature in jarosite.

■ RESULTS AND DISCUSSION

Structural Characterization. Initial experiments focused on elucidating the structure of jarosite at high pressure using powder and single crystal X-ray diffraction (PXRD, SCXRD) to enable a structure−function correlation. Jarosite's high-pressure crystal structure provides detailed information about potential magnetic coupling pathways, the spin state of the Fe ion, and the integrity of the kagomé lattice via the bond metrics. There are three crystallographic pathways important to the magnetic structure: the dominant antiferromagnetic Fe−O−Fe coupling path in the kagomé plane, the hypothesized interlayer superexchange Fe−O−K−O−Fe path, and the hypothesized interlayer superexchange Fe−O−S−O···H−O−Fe path, which includes a hydrogen bond. For simplicity, the three pathways will be referred to as the Fe−O−Fe pathway, the four-member pathway, and the six-member pathway, respectively.

To ascertain the integrity of these three coupling pathways at high pressure, we acquired room temperature single-crystal structures for jarosite at 16.2, 26.3, and 30.9 GPa using synchrotron SCXRD (Figure 1 and Table S4 in the Supporting Information). The single-crystal data are well modeled in the

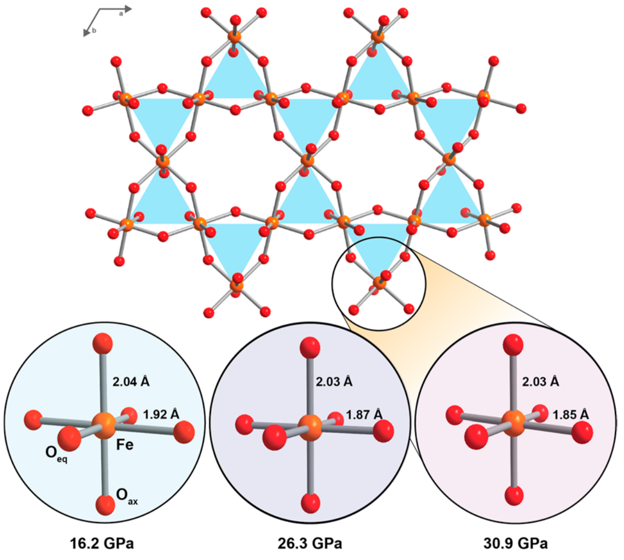

Figure 1. Crystal structure of jarosite at 30.9 GPa featuring a kagomé lattice of iron atoms in the *ab* crystallographic plane (top). The lattice is highlighted by the light blue triangles. Iron and oxygen ions are denoted by orange and red spheres, respectively. The sulfate and potassium ions are omitted for clarity. Hydrogen atoms were not included in the structural refinement. Circles highlight refined structures of FeO_6 iron−oxygen pseudooctahedra at pressures of 16.2, 26.3, and 30.9 GPa (bottom). The two apical oxygen atoms point out of the kagome layer, while the equatorial oxygen atoms lie within the *ab* plane. The Fe−O_{ax} and Fe−O_{eq} bond distances are labeled in the figure for each pressure.

DOI: 10.1021/jacs.8b05601
J. Am. Chem. Soc. 2018, 140, 12001−12009

space group $R\bar{3}m$ at all three pressures. The Fe−O bond distances in the FeO_6 pseudooctahedra decrease with increasing pressures (Figure 1, bottom). The equatorial Fe−O bond distance shrinks from 1.993(3) Å in the ambient pressure structure[10] to 1.92(1) Å, then 1.87(2) Å, and finally to 1.85(2) Å in the 16.2, 26.3, and 30.9 GPa structures, respectively. Similarly, the axial Fe−O bond distance drops from 2.0623(5) Å in the ambient pressure structure to 2.04(2) Å, then to 2.03(4) Å in the 16.2 and 26.3 GPa structures, respectively, and remains at this value within error in the 30.9 GPa structure. Importantly, the Fe−O−Fe angle in the kagomé planes remains relatively invariant. The O−O distance, which serves as a proxy for the hydrogen bond distance and strength, drops precipitously between ambient pressure and 16.2 GPa, from 2.908(4) Å to 2.55(1) Å, and then decreases very slowly with pressure, to 2.54(3) Å at 26.3 GPa and then to 2.52(3) Å at 30.9 GPa. Last, the interlayer spacing decreases from 5.7125 to 5.1961 Å, then to 5.060 Å, and then to 5.034 Å as pressure increases. These crystal structures show that, over 30.9 GPa, the three coupling pathways in question remain intact, that the interlayer spacing decreases by ~0.7 Å, and that the $Fe-O_{eq}$ bonds contract by almost 0.15 Å while the $Fe-O_{ax}$ bonds remain relatively invariant.

Pressure-induced phase transitions manifest as a deviation of the unit-cell parameters from a single third-order Birch−Murnaghan equation of state curve.[20,21] To probe the possibility of pressure-induced phase transitions, and to investigate the change in the interlayer spacing more thoroughly, we collected PXRD patterns using synchrotron radiation at pressures up to 36.2 GPa (Figure 2, and Supporting Information Figures S3−S7, also see the Supporting Information for a discussion of the patterns).[22] Discontinuities in the pressure dependence of the unit cell parameters near 20 GPa, and again near 30 GPa, suggest a gradual phase transition over this pressure range. We fitted these data to an error-weighted least-squares third-order Birch−Murnaghan equation of state to further explore these discontinuities (see Supporting Information for all equation of state parameter values). At pressures up to 19.8 GPa, one equation of state curve accurately models the data. Above 19.8 GPa, the data smoothly and continuously drift away from this equation of state curve. A second equation of state curve accurately models the data between 29.6 and 36.2 GPa. The weighted-χ^2 values for the low- and high-pressure volume equations of state are 1.15 and 0.93, respectively, while the weighted-χ^2 value for a single equation of state fit to the entire pressure range is 13.1. The significant change in fit quality demonstrates that, to be modeled accurately, the data require two equation of state curves. This confirms a continuous transition between 19.8 and 29.6 GPa from a low-pressure to a new, high-pressure phase.

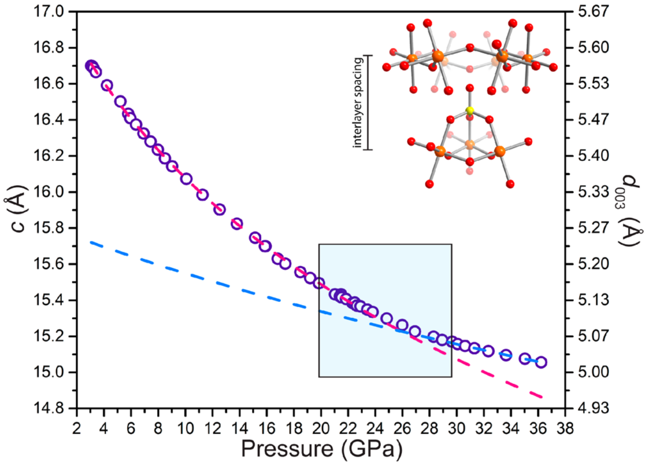

Figure 2. Continuous phase change in jarosite between 20 and 30 GPa revealed by variable-pressure PXRD studies, as shown by a change in the unit cell c-axis parameter. The circles plot the raw data. The error bars in c and in pressure are smaller than the symbols. The red and blue dashed lines represent low-pressure and high-pressure Birch−Murnaghan third-order equation of state curves, respectively. The right-hand vertical axis shows the interlayer spacing. The light blue box highlights jarosite's pressure-induced continuous phase change. The inset shows one sulfate-capped $\{Fe_3\}$ equilateral triangle positioned below the hexagonal pore in the layer above it. Iron, oxygen, and sulfur ions are denoted by orange, red, and yellow spheres, respectively. The interlayer spacing is noted by the capped line to the left of the inset, which is not to scale. Potassium atoms are ommited for clarity. Hydrogen atoms were excluded from the structure refinement.

One key difference between these two phases is the compressibility along the c-axis, which changes across the phase transition. This affects the change in the interlayer spacing with pressure, which derives from the length of the c-axis. The Fe ions occupy special positions in the unit cell such that there are three kagomé layers per unit cell; therefore, the interlayer spacing is one-third of the c-axis length. Here, the interlayer spacing decreases from 5.7125 Å at ambient pressure to 5.019 Å at 36.2 GPa. Notably, the interlayer spacing decreases much more rapidly with pressure below 20 GPa than it does above 30 GPa.

The PXRD data and the three SCXRD structures demonstrate that the kagomé lattice remains intact with no reduction in symmetry in the system through the continuous pressure-induced phase transition. However, the crystallographic studies thus far omit the hydrogen atoms in jarosite. A change in the nature of the hydrogen bonding could give rise to a subtle structural change. There is precedent in the high-pressure literature for this kind of transition, for example, in iron oxyhydroxide at approximately 16 GPa.[23−25] Previous studies attribute the transition in iron oxyhydroxide to a stiffening of the hydrogen bonds.[23] Our PXRD data, and the change in the O−O interaction distances derived from the SCXRD data, closely resemble their crystallographic data around 16 GPa. Therefore, we hypothesized that the continuous phase transition in jarosite between 20 and 30 GPa arises from a stiffening of the interlayer hydrogen bonds.

To test this hypothesis, we conducted variable-pressure Raman spectroscopy experiments up to 29.1 GPa. We focused our efforts on the high wavenumber shift region, between 3000 and 4000 wavenumbers. Three O−H modes are observable in this region in jarosite close to ambient pressure (Figure 3).[26,27] The modes move to lower Raman shift as a function of pressure. At approximately 18 GPa, the rate at which the modes shift as a function of pressure decreases (see Supporting Information Figure S18). This mode stiffening and the relatively low Raman shift values for these three modes indicate very strong hydrogen bonding interactions.[25] These data support the above hypothesis by showing that, at approximately 18 GPa, the nature of the hydrogen bonding changes subtly. Above this pressure, the hydrogen bonds become significantly less compressible. We hypothesize that

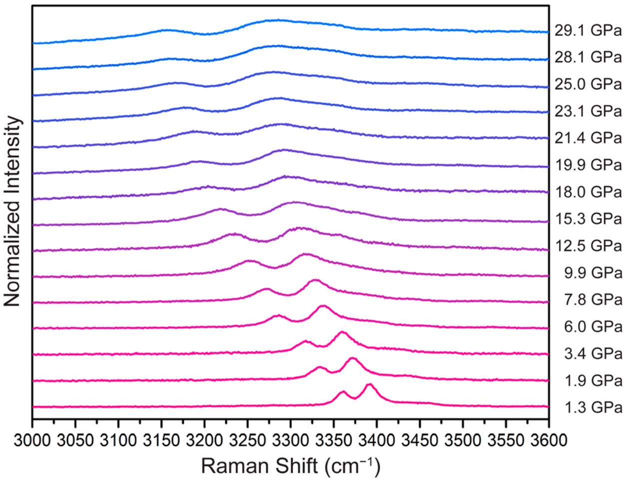

Figure 3. Three O−H modes visible in the low-pressure Raman spectrum for jarosite. These modes are at approximately 3360, 3390, and 3450 cm^{-1}, respectively. As pressure increases, these modes decrease in Raman shift, indicating strong hydrogen bonding interactions. At approximately 18 GPa, the modes stiffen. They continue to decrease in Raman shift with pressure, but at a slower rate. The relatively low Raman shift value for these hydrogen bonds, and the mode stiffening, support strong hydrogen bonding interactions that increase in strength with increasing pressure.

this behavior causes the continuous, isostructural phase transition observed in the PXRD data.

Magnetic Characterization. To probe the magnetic properties of jarosite under pressure, we acquired SQUID-based magnetometry data, time-domain synchrotron Mössbauer spectroscopy (SMS) data, and X-ray magnetic circular dichroism (XMCD) data. Our initial studies used SQUID magnetometry to obtain temperature-dependent magnetic susceptibility measurements (Figure 4, left) up to 1.32 GPa. These data show a monotonic increase in the Néel temperature from 65 to 70.9 K as pressure increases from ambient pressure to 1.32 GPa. To extend the accessible pressure ranges of this magnetic study, we turned to techniques that are compatible with diamond anvil cells.

We conducted variable-temperature and -pressure SMS experiments on a single crystal of jarosite to probe the magnetic properties of jarosite's high pressure phase. SMS is a time-domain technique that uses pulsed synchrotron radiation to probe the nuclear spin transition of Fe.[28,29] As such, it yields similar information to Mössbauer spectroscopy. Fits of these data yield the magnetic hyperfine parameter (B_{HF}) at each temperature and pressure (see Supporting Information Figures S9−S13 for plots of the data and fits, and Table S5 for the fit parameter values). B_{HF} comprises four terms: the Fermi contact term, the spin−orbit term, the dipolar term, and the applied magnetic field term.[30,31] In general, and in our system, the Fermi contact term dominates and B_{HF} is a good proxy for the onset of magnetic ordering. That is, magnetic order gives rise to a nonzero B_{HF}. The plot of B_{HF} vs temperature (Figure 4, right) shows that the onset of a nonzero B_{HF}, and therefore the magnetic ordering temperature, increases monotonically as a function of pressure.

The data from the SQUID-based magnetometry, the SMS, and the XMCD experiments form the magnetic phase diagram for jarosite (Figure 4, center). The SQUID magnetometry data provide the Néel temperature for jarosite up to 1.32 GPa. Above that pressure, the SMS data provide the magnetic ordering temperatures as signaled by the onset of a nonzero B_{HF}. We assume that the onset of a nonzero B_{HF} marks the Néel temperature for two reasons. First, XMCD data obtained for jarosite at ambient pressure at 1.5 K and at 38.6 GPa at 1.5 K (discussed in the Supporting Information and plotted in Figures S14 and S15) demonstrate that this magnetic ordering temperature is not a Curie temperature. Second, the material

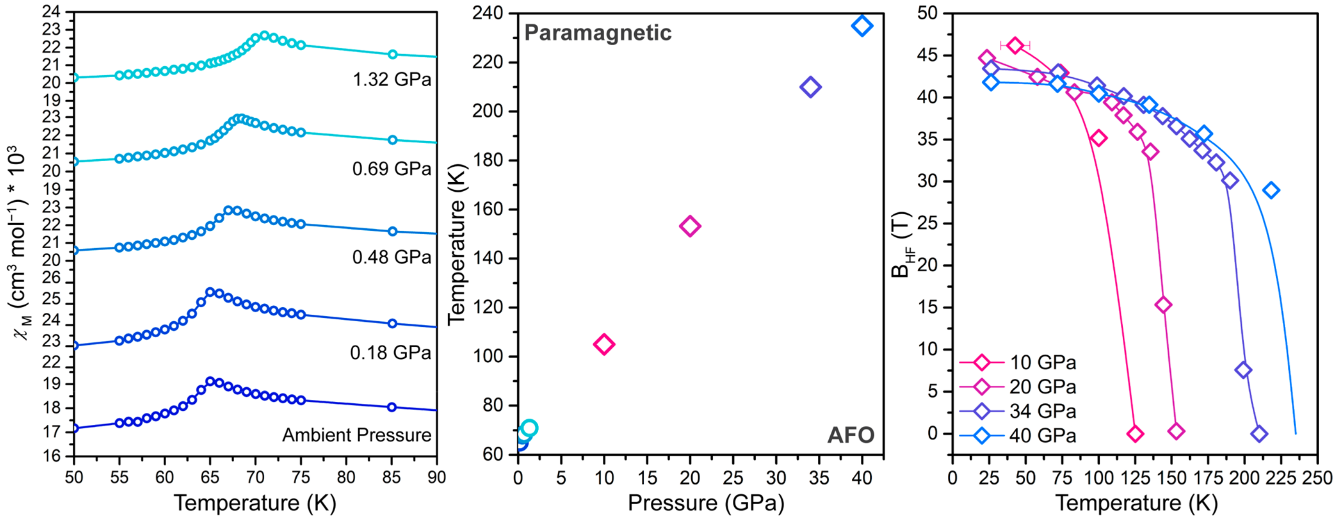

Figure 4. Plot of magnetic susceptibility showing the increase in Néel temperature as a function of pressure (left). The plot of B_{HF} vs temperature (right) highlights the onset of magnetic ordering in jarosite as a function of pressure. The solid lines are splines intended to guide the eye. At the highest pressure, the spline is extrapolated to a potential x intercept to obtain an approximate magnetic ordering temperature for that pressure. Jarosite's magnetic phase diagram as a function of pressure (center) derives from the magnetic ordering temperatures obtained from the magnetometry and the SMS data. The Néel temperatures derived from the magnetometry data are plotted as circles, and the ordering temperatures derived from the SMS data are plotted as diamonds. The magnetic ordering temperature increases linearly (adjusted-R^2 = 0.9996) with pressure. Below these temperatures, we hypothesize that the material orders antiferromagnetically. For all plots, the error bars are smaller than the symbols if they are not shown.

DOI: 10.1021/jacs.8b05601
J. Am. Chem. Soc. 2018, 140, 12001−12009

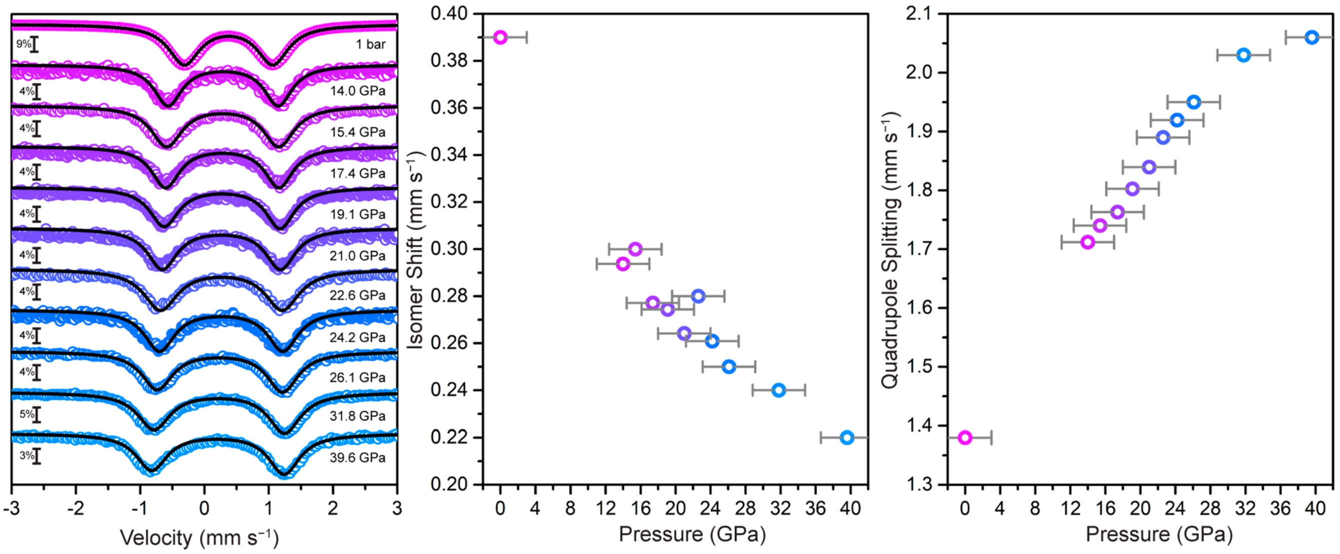

Figure 5. Mössbauer spectra at increasing pressures (left). The colored, empty circles are the data at each pressure, and the black lines are the corresponding fits of these data. The corresponding scale bars and pressures are beneath each of the spectra. The isomer shift and quadrupole splitting values derive from the fits. The evolution of the isomer shift (middle) and the quadrupole splitting (right) as a function of pressure are shown. The symbols are larger than the error bars in the isomer shift and quadrupole splitting.

remains in the same space group throughout the pressure range, and through the structural transition. Indeed, the SCXRD experiments show that the material remains remarkably structurally similar through and above the phase transition. Therefore, we extend the same Goodenough−Kanamori arguments that rationalize the ambient pressure antiferromagnetic order to the high-pressure phase.[5,10,32,33] The orbital coupling pathways remain intact, and the orbital electronic occupation remains constant, such that the critical temperature shown via SMS is a Néel temperature according to the Goodenough−Kanamori rules.

The aggregate of the magnetometry, the SMS, and the XMCD data show that the Néel temperature increases smoothly as a function of pressure. In fact, a linear fit to the ordering temperatures derived from these techniques gives an adjusted-R^2 value of 0.9996, indicating that the Néel temperature increases linearly as a function of pressure. Therefore, the magnetic behavior of the high-pressure phase of jarosite is relatively unaffected by the phase transition in the material.

Electronic Structure Characterization. To probe the electronic structure of jarosite at elevated pressures, we utilized Mössbauer, X-ray emission spectroscopy (XES), and UV−vis spectroscopy as well as optical microscopy. Mössbauer spectroscopy provides indirect, local information about the electronic and structural properties of an ion in a compound through the quadrupole splitting (ΔE_Q) and isomer shift (δ) parameters. Here, the two parameters provide information pertaining to the local structural and electronic environment around the Fe^{3+} ions. We measured a crystalline powder of jarosite enriched to 20% ^{57}Fe at ambient temperature and at pressures up to 39.6 GPa (Figure 5, left). Fitting the data at each pressure yielded δ and ΔE_Q values (Figure 5, center and right, respectively). The ΔE_Q and δ values at ambient pressure are typical for jarosite;[34,35] the relatively high ambient pressure ΔE_Q value is accounted for by considering lattice contributions.[36] As pressure increases, ΔE_Q increases monotonically while δ decreases. The decrease in δ mirrors the decrease in $Fe{-}O_{eq}$ bond length. As the bond length shortens, the covalent nature of the bond increases and more electron density from the Fe ion is shared into the four equatorial $Fe{-}O_{eq}$ bonds. Correspondingly, δ decreases. The pressure-induced increase in ΔE_Q marks the increased asymmetry in the Fe^{3+} coordination sphere. As pressure increases, the axial elongation in the FeO_6 pseudooctahedra becomes substantially more pronounced, which leads to the increase in ΔE_Q.

There is a small inflection point in the ΔE_Q vs pressure plot at 31.8 GPa, which may signal a transition in jarosite's electronic structure. One such transition is a pressure-induced spin crossover; however, these transitions generally cause first order discontinuities in both Mössbauer parameters in materials that contain $Fe^{3+}O_6$ moieties.[37−40] Alternatively, it may result from an increase in the symmetry of the Fe^{3+} coordination sphere induced by the stiffening of the hydrogen bonds. As pressure increases, the interlayer void space disappears. After void space, the most compressible moieties along the *c*-axis are the hydrogen bonds. Once the hydrogen bonds stiffen—above the pressure-induced continuous phase change observed in the PXRD—the $Fe{-}O_{ax}$ bonds begin to compress with pressure. The compression of the $Fe{-}O_{ax}$ bonds decreases the degree of the axial elongation in the pseudooctahedra, giving rise to an inflection point in the ΔE_Q plot at 31.8 GPa. Above the inflection point, the rate of change of ΔE_Q with pressure decreases. Thus, these data suggest that the small inflection point in the ΔE_Q plot originates from both electronic and structural changes. It should be noted that this analysis relies upon only one data point. A more thorough investigation may further test the conclusions herein concerning the inflection point in the ΔE_Q data. From the clean doublet in these data (Figure 5, left), we conclude that one chemically distinct Fe site is present throughout the pressure range.

To better understand the electronic structure of jarosite at high applied pressures, we turned to nonresonant XES measurements at the Fe K-edge. Three key features arise in these spectra: the main $K\beta$ line at approximately 7060 eV, the $K\beta'$ feature at approximately 7045 eV, and a shoulder on the low energy side of the $K\beta$ feature.[41,42] The entire spectrum is uniquely sensitive to the Fe ions' electronic structure. The $K\beta'$ feature is diagnostic of the Fe centers' spin state, as the intensity of that feature is directly proportional to the number of unpaired spins in the 3d orbitals via the exchange interaction. We collected variable-pressure XES data on three different samples of crystalline jarosite up to 40 GPa. Figure 6 shows the lowest and highest-pressure data collected from one of these samples. At high pressures, the $K\beta$ feature shifts to lower energy, and the intensity of the $K\beta'$ feature decreases. An increase in the covalent nature of the Fe–O bonds as a function of pressure gives rise to these changes.[43] To further examine the change in the electronic structure as a function of pressure, we treated the data collected from each sample independently using the integral of the absolute value of the difference curves (IAD) method (Figure 6 inset).[44] This method quantifies subtle changes in the spectra which in turn gives information about the change in the electronic structure of the material. The IAD values vary almost linearly with pressure (adjusted-R^2 = 0.9752). If a pressure-induced phase transition in the electronic structure existed, it would be apparent as a discontinuity in the plot of the IAD as a function of pressure. These data, therefore, offer very strong evidence that the changes in jarosite's electronic structure arise solely from an increase in covalency in the Fe–O bonds. They highlight the linear nature of the increase in Fe–O covalency as a function of pressure, which mirrors the nature of the decrease in the Fe–O bond length.

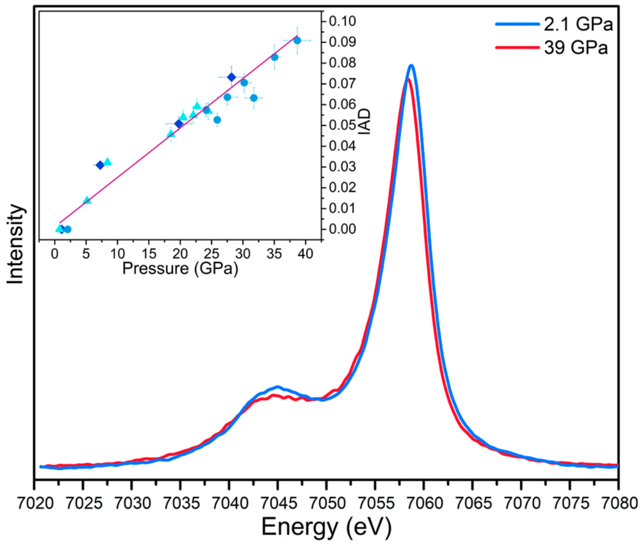

Figure 6. XES spectra for jarosite at 2.1 and 39 GPa are plotted as blue and red lines, respectively. The inset shows the IAD values for all of the spectra. The error bars are 3σ of the absolute value of the differene curves. The error bars for the pressure values are estimated based on the measured pressure differential in high pressure diamond anvil cells. The data from the three samples measured are represented as triangles, circles, and diamond symbols. The solid line is a fit to these data. All of the IAD values fall roughly on the same line (adjusted-R^2 = 0.9752).

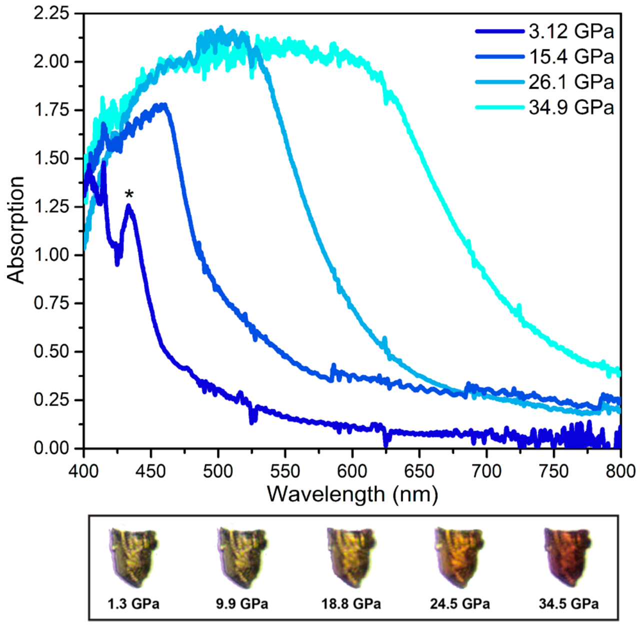

Figure 7. Variable pressure UV–vis absorption spectra. These spectra display a feature at approximately 433 nm which grows in intensity and red shifts slightly as pressure increases to 15.4 GPa (top). Above approximately 19 GPa, the features widens to give one large, flat feature in the UV and visible regions. The starred feature is assigned as the $^6A_{1g}$ to $^4E_g,^4A_{1g}$ transitions. The single crystal of jarosite exhibits piezochromism (bottom).

We corroborated the X-ray spectroscopy-based evidence using optical microscopy and UV–vis spectroscopy. UV–vis spectroscopy yields detailed information about electronic transitions and thus information about electronic structure. We collected UV–vis data as a function of pressure on a single crystal of jarosite up to 34.9 GPa (Figure 7, top; Figure S17 in the Supporting Information). At 3 GPa, the spectrum agrees well with the ambient pressure data previously reported for jarosite.[45,46] We assign the sharp red feature of the UV absorption band, at approximately 433 nm, as the $^6A_{1g}$ to $^4E_g,^4A_{1g}$ transition (denoted as the ($^4E_g,^4A_{1g}$) band) in accordance with the previous studies of this mineral.[47] The observation of the 433 nm sharp feature confirms that the light is incident along the surface normal to the basal plane.[45] The $^6A_{1g}$ to $^4T_{1g}$ transition (denoted as the $^4T_{1g}$ band) occurring near 900 nm, reported at ambient conditions, cannot be unambiguously identified in this work because of the inherent limits of the accessible spectral range and signal strength. The strong absorption in the purple and blue portion of the visible range renders the jarosite crystal pale yellow to the eye (Figure 7, bottom). The ($^4E_g,^4A_{1g}$) band red shifts and grows in intensity as a function of pressure from 3 GPa up to approximately 19 GPa. At 19 GPa, the originally discrete and sharp absorption peak merges with the broad continuous feature on its high energy side. Above 19 GPa, up to 34.9 GPa, the feature widens and the edge continues to red shift. Notably, this absorption band exhibits a largely featureless, flat plateau at its maximum. The edge of this broad absorption band steadily red shifts with increasing pressure. As the absorption edge moves into the green portion of the visible range and then into the near-IR, the jarosite crystal becomes dark red (Figure 7, bottom). We tentatively attribute this behavior to a smooth decrease of the bandgap. The Fe–O orbital overlap increases with pressure, which causes an increase in the energy of the $d_{x^2-y^2}$ orbital and therefore a presumed decrease between the $d_{x^2-y^2}$ orbital and the LUMO, which form the valence band and the conduction band, respectively (see Figure S19 in the Supporting Information).

The UV−vis and XES measurements show that jarosite's electronic structure varies continuously and smoothly as a function of pressure. They show that no phase change in the electronic structure accompanies the observed structural transition. These measurements corroborate the interpretation of the structural and magnetic data above.

Magnetostructural Correlation. The structural, magnetic, and electronic characterizations help to elucidate the evolution of the different magnetic coupling interactions in jarosite as a function of pressure. The important magnetic coupling interactions present in jarosite at ambient pressure are the intralayer antiferromagnetic Fe−O−Fe interaction in the kagomé plane, the interlayer four-member superexchange pathway, and the interlayer six-member superexchange pathway. Currently, hypotheses state that interlayer coupling manifests via a dipolar interaction and that the superexchange pathways may play some secondary role in 3D magnetic ordering.[10,48] Above and near the Néel temperature, the DM interaction groups the Fe ions into triangular spin plaquettes. Then, 2D correlation develops in which neighboring triangular spin plaquettes align ferromagnetically within a plane. As the temperature in the system reaches the Néel temperature, the regions of 2D correlation within individual layers couple via the dipolar interaction, and 3D magnetic order arises.

Substitutional studies in the literature that vary the cation in Fe jarosite illustrate that the Néel temperature is invariant with respect to the interlayer spacing.[17] It was shown that, when the cation varies from Rb^+ to Ag^+, the interlayer spacing decreases from 5.934(5) Å to 5.498(3) Å. Despite the approximately 0.44 Å decrease in interlayer spacing, the Néel temperature decreases from 65.1 to 59.7 K, in contrast to the trend observed in our data. Additionally, a vast series of cation-substituted Fe jarosite congeners exists. In this family, the cations include K^+, Na^+, Rb^+, Ag^+, Tl^+, NH_4^+, $0.5Pb^{2+}$, and H_3O^+. There is no trend in the Néel temperature in this family of Fe jarosite compounds as a function of the cation-induced change in the interlayer spacing.[10,17] However, while the interlayer spacing in these compounds varies by more than 0.4 Å, the bond metrics in the Fe^{3+} coordination sphere are nearly identical across the series. In contrast, our data show that the Néel temperature increases by approximately 180 K, which is more than an order of magnitude larger than the change observed between the Rb^+ and Ag^+ jarosite congener end members. In our system, the increase in Néel temperature occurs as we increase pressure smoothly from ambient pressure to almost 40 GPa, which corresponds to a nonlinear decrease in interlayer spacing of ∼0.7 Å. More importantly, the $Fe-O_{eq}$ bond length decreases by ∼0.15 Å between ambient pressure and 30.9 GPa. The $Fe-O_{eq}$ bond distance decreases nearly linearly with pressure: a linear fit of the $Fe-O_{eq}$ bond distances as a function of pressure gives an adjusted-R^2 value of 0.9914, with a slope of −0.47 pm/GPa. Additionally, from the pressure-induced changes in the ΔE_Q and δ values, and from the IAD analysis of the XES data, we see that the degree of Fe−O covalency increases nearly linearly across this pressure range.

We conclude that the onset of magnetic order stems directly from the strength of the intralayer Fe−O−Fe antiferromagnetic superexchange interaction, the magnitude of which increases with increasing $Fe-O_{eq}$ covalency. Increased pressures lead to a nearly linear increase in the degree of $Fe-O_{eq}$ covalency (decrease in bond length, decrease in δ, increase in IAD value) in the Fe−O−Fe pathway, which directly strengthens the antiferromagnetic coupling. Additionally, the DM interaction is proportional to the hopping integral, which is in turn proportional to metal−ligand covalency.[17,49−52] The increase in strength of these magnetic interactions increases the temperature at which the DM interaction binds the electronic spins in an Fe^{3+} triangle into a correlated triangular spin plaquette, which raises the temperature at which large 2D correlated areas in the kagomé layers exist. This leads to a linear increase in the Néel temperature with pressure, even with a nonlinear decrease of the interlayer spacing. We find that the magnitude of the through-space interlayer dipolar coupling interaction is independent of any change in the interlayer spacing between 5.034 and 5.934(5) Å.

■ CONCLUSION

In conclusion, we conducted the first in-depth study of jarosite's structural, electronic, and magnetic properties at high applied pressures. This study revealed a continuous pressure-induced phase transition without a change in Fe^{3+} spin state or break in symmetry from the kagomé lattice. Using Raman spectroscopy, we showed that the phase change may arise from a stiffening of the hydrogen bonds. Intrigued by whether the phase transition induced changes in the magnetic or electronic structure, we combined several techniques to complete thorough electronic and magnetic studies of jarosite's high pressure phase. We observed an increase in metal−ligand covalency that was concomitant with an increase in the Néel temperature, which itself is nearly linear as a function of pressure. From these data, we formed a chemically pure magnetostructural correlation that sheds light on the nature of 3D magnetic order in jarosite. We untangled the disparate magnetic coupling interactions in jarosite and propose that an increase in metal−ligand covalency dictates the magnetic ordering temperature, and not the interlayer spacing. In doing so, we demonstrated that high pressure enables chemically pure structure−function correlation. Analogous with extremely low temperatures or extremely high magnetic fields, high pressure unlocks an uncharted region of electronic and magnetic phase space. Magnetism at high pressure is an emerging area of research, and the aggregate of the measurements presented herein demonstrate the power of applying high-pressure techniques to chemical questions.

■ ASSOCIATED CONTENT

Ⓢ Supporting Information

The Supporting Information is available free of charge on the ACS Publications website at DOI: 10.1021/jacs.8b05601.

Full experimental details and additional data (PDF)

■ AUTHOR INFORMATION

Corresponding Author

*danna.freedman@northwestern.edu

ORCID

Yinsheng Guo: 0000-0002-0571-8447
Richard P. Van Duyne: 0000-0001-8861-2228
Steven D. Jacobsen: 0000-0002-9746-958X
Danna E. Freedman: 0000-0002-2579-8835

Notes

The authors declare no competing financial interest.

ACKNOWLEDGMENTS

This experimental work on creating materials is supported by the AFOSR (FA9550-17-1-0247). Research on kagomé lattices is supported by ARO (W911NF1810006). The collaborative project between D.E.F and S.D.J. is supported by Northwestern University through the Innovative Initiatives Incubator (I3) and supports J.P.S.W. We thank S. Coste, Dr. J. Lazarz, M. Wenz, Dr. M. Graham, and Prof. J. Zadrozny for their insightful comments. We thank Drs. S. N. Tkachev, D. Zhang, and C. Kenney-Benson for technical support. S.M.C. acknowledges support from the NSF GRFP (DGE-1324585). S.D.J. acknowledges support from the Carnegie/DOE Alliance Center (CDAC), the NSF (EAR-1452344), and the David and Lucile Packard Foundation. W.B. is partially supported by the Consortium for Materials Properties Research in Earth Sciences (COMPRES). The UV−vis spectroscopy work was supported by NSF Grant CHE1506683. The DOE-NNSA Award No. DE-NA0001974 and DOE-BES Award No. DE-FG02-99ER45775 support HPCAT, and the NSF provides partial funding for instrumentation. The National Science Foundation−Earth Sciences (EAR-1634415) and Department of Energy−Geosciences (DE-FG02-94ER14466) support GSECARS. The gas loading was also partially supported by COMPRES under the NSF Cooperative Agreement EAR 1606856. Experiments at Sector 13-BM-C were conducted under the Partnership for Extreme Crystallography (PX∧2), also supported by COMPRES. The APS is a U.S. Department of Energy (DOE) Office of Science User Facility operated for the DOE Office of Science by Argonne National Laboratory under Contract No. DE-AC02-06CH11357. This work made use of the IMSERC facility at NU, supported by NSF NNCI-1542205; the Keck Foundation; the State of Illinois; and the IIN.

REFERENCES

(1) Elwood Madden, M. E.; Bodnar, R.; Rimstidt, J. *Nature* **2004**, *431* (7010), 821.

(2) Klingelhöfer, G.; Morris, R. V.; Bernhardt, B.; Schröder, C.; Rodionov, D. S.; de Souza, P. A., Jr.; Yen, A.; Gellert, R.; Evlanov, E. N.; Zubkov, B.; Foh, J.; Bonnes, U.; Kankeleit, E.; Gütlich, P.; Ming, D. W.; Renz, F.; Wdowiak, T.; Squyres, S. W.; Arvidson, R. E. *Science* **2004**, *306*, 1740−1745.

(3) Bigham, J.; Schwertmann, U.; Traina, S.; Winland, R.; Wolf, M. *Geochim. Cosmochim. Acta* **1996**, *60* (12), 2111−2121.

(4) Squyres, S.; Grotzinger, J.; Arvidson, R.; Bell, J.; Calvin, W.; Christensen, P.; Clark, B.; Crisp, J.; Farrand, W.; Herkenhoff, K. E.; Knoll, A. H.; McLennan, S. M.; McSween, H. Y., Jr.; Morris, R. V.; Rice, J. W., Jr.; Rieder, R.; Soderblom, L. A.; Johnson, J. R.; Klingelhofer, G. *Science* **2004**, *306* (5702), 1709−1714.

(5) Grohol, D.; Matan, K.; Cho, J.-H.; Lee, S.-H.; Lynn, J. W.; Nocera, D. G.; Lee, Y. S. *Nat. Mater.* **2005**, *4*, 323−328.

(6) de Vries, M.; Johal, T.; Mirone, A.; Claydon, J.; Nilsen, G.; Rønnow, H.; van der Laan, G.; Harrison, A. *Phys. Rev. B: Condens. Matter Mater. Phys.* **2009**, *79*, 045102.

(7) Matan, K.; Grohol, D.; Nocera, D. G.; Yildirim, T.; Harris, A. B.; Lee, S. H.; Nagler, S. E.; Lee, Y. S. *Phys. Rev. Lett.* **2006**, *96*, 247201.

(8) Grohol, D.; Nocera, D. G. *J. Am. Chem. Soc.* **2002**, *124*, 2640−2646.

(9) Nocera, D. G.; Bartlett, B. M.; Grohol, D.; Papoutsakis, D.; Shores, M. P. *Chem. - Eur. J.* **2004**, *10*, 3850−3859.

(10) Grohol, D.; Nocera, D. G.; Papoutsakis, D. *Phys. Rev. B: Condens. Matter Mater. Phys.* **2003**, *67* (6), 64401.

(11) Bartlett, B. M.; Nocera, D. G. *J. Am. Chem. Soc.* **2005**, *127*, 8985−8993.

(12) Grochala, W.; Hoffmann, R.; Feng, J.; Ashcroft, N. W. *Angew. Chem., Int. Ed.* **2007**, *46* (20), 3620−3642.

(13) Zhang, L.; Wang, Y.; Lv, J.; Ma, Y. *Nat. Rev. Mater.* **2017**, *2* (4), 17005.

(14) Wang, Y.; Zhou, Z.; Wen, T.; Zhou, Y.; Li, N.; Han, F.; Xiao, Y.; Chow, P.; Sun, J.; Pravica, M.; Cornelius, A. L.; Yang, W.; Zhao, Y. *J. Am. Chem. Soc.* **2016**, *138* (48), 15751−15757.

(15) Gütlich, P.; Garcia, Y.; Goodwin, H. A. *Chem. Soc. Rev.* **2000**, *29* (6), 419−427.

(16) Gütlich, P.; Gaspar, A. B.; Garcia, Y. *Beilstein J. Org. Chem.* **2013**, *9*, 342.

(17) Jaffe, A.; Lin, Y.; Mao, W. L.; Karunadasa, H. I. *J. Am. Chem. Soc.* **2015**, *137* (4), 1673−1678.

(18) Yadav, R.; Rachel, S.; Hozoi, L.; van den Brink, J.; Jackeli, G. Pressure-Tuned Magnetic Interactions in Honeycomb Kitaev Materials. arXiv preprint arXiv:1802.01051. **2018**.

(19) Goncharov, A. F.; Struzhkin, V. V.; Mao, H.; Hemley, R. J. *Phys. Rev. Lett.* **1999**, *83* (10), 1998.

(20) Murnaghan, F. D. *Proc. Natl. Acad. Sci. U. S. A.* **1944**, *30*, 244−247.

(21) Birch, F. *Phys. Rev.* **1947**, *71* (11), 809.

(22) The equation of state of jarosite is known up to 8.1 GPa. It is published in Xu, H.; Zhao, Y.; Zhang, Y.; Hickmott, D. D.; Daemen, L. L.; Hartl, M. A.; Wang, L.; Wang, Y. *Am. Mineral.* **2010**, *95*, 19−23.

(23) Xu, W.; Greenberg, E.; Rozenberg, G. K.; Pasternak, M. P.; Bykova, E.; Boffa-Ballaran, T.; Dubrovinsky, L.; Prakapenka, V.; Hanfland, M.; Vekilova, O. Y.; Simak, S. I.; Abrikosov, I. A.; et al. *Phys. Rev. Lett.* **2013**, *111* (17), 175501.

(24) Friedrich, A.; Wilson, D.; Haussühl, E.; Winkler, B.; Morgenroth, W.; Refson, K.; Milman, V. *Phys. Chem. Miner.* **2007**, *34* (3), 145−157.

(25) Gleason, A. E.; Jeanloz, R.; Kunz, M. *Am. Mineral.* **2008**, *93* (11−12), 1882−1885.

(26) Sasaki, K.; Tanaike, O.; Konno, H. *Can. Mineral.* **1998**, *36*, 1225−1235.

(27) Frost, R. L.; Wills, R.-A.; Weier, M. L.; Martens, W. *J. Raman Spectrosc.* **2005**, *36* (5), 435−444.

(28) Sturhahn, W. *J. Phys.: Condens. Matter* **2004**, *16*, S497.

(29) Alp, E.; Mooney, T.; Toellner, T.; Sturhahn, W. *Hyperfine Interact.* **1994**, *90*, 323.

(30) Gibb, T. C. *Principles of Mössbauer Spectroscopy*; Springer, 2013; pp 109−118.

(31) Dickson, D. P.; Berry, F. J. *Mössbauer Spectroscopy*; Cambridge University Press, 2005; pp 143−197.

(32) Goodenough, J. B. *Phys. Rev.* **1955**, *100* (2), 564.

(33) Kanamori, J. *J. Phys. Chem. Solids* **1959**, *10* (2−3), 87−98.

(34) Leclerc, A. *Phys. Chem. Miner.* **1980**, *6*, 327−334.

(35) Stevens, J. G.; Khasanov, A. M.; Miller, J. W.; Pollak, H.; Li, Z. *Mössbauer Mineral Handbook*; Biltmore Press: Asheville, NC, 1998.

(36) Hrynkiewicz, A. Z.; Kubisz, J.; Kulgawczuk, D. S. *J. Inorg. Nucl. Chem.* **1965**, *27*, 2513−2517.

(37) Greenberg, E.; Rozenberg, G. K.; Xu, W.; Pasternak, M. P.; McCammon, C.; Glazyrin, K.; Dubrovinsky, L. S. *Phys. Rev. B: Condens. Matter Mater. Phys.* **2013**, *88* (21), 214109.

(38) Xu, W.; Naaman, O.; Rozenberg, G. K.; Pasternak, M.; Taylor, R. *Phys. Rev. B: Condens. Matter Mater. Phys.* **2001**, *64* (9), 94411.

(39) Arielly, R.; Xu, W.; Greenberg, E.; Rozenberg, G. K.; Pasternak, M.; Garbarino, G.; Clark, S.; Jeanloz, R. *Phys. Rev. B: Condens. Matter Mater. Phys.* **2011**, *84* (9), 94109.

(40) Pasternak, M.; Rozenberg, G. K.; Machavariani, G. Y.; Naaman, O.; Taylor, R.; Jeanloz, R. *Phys. Rev. Lett.* **1999**, *82* (23), 4663.

(41) De Groot, F. *Chem. Rev.* **2001**, *101* (6), 1779−1808.

(42) Glatzel, P.; Bergmann, U.; de Groot, F. M.; Cramer, S. P. *Phys. Rev. B: Condens. Matter Mater. Phys.* **2001**, *64* (4), 45109.

(43) Pollock, C. J.; Delgado-Jaime, M. U.; Atanasov, M.; Neese, F.; DeBeer, S. *J. Am. Chem. Soc.* **2014**, *136* (26), 9453−9463.

(44) Vankó, G.; Rueff, J.-P.; Mattila, A.; Németh, Z.; Shukla, A. *Phys. Rev. B: Condens. Matter Mater. Phys.* **2006**, *73* (2), 24424.

(45) Rossman, G. R. *Am. Mineral.* **1976**, *61* (5−6), 398−404.

(46) Rossman, G. R.; Dyar, M.; McCammon, C.; Schaefer, M. Why Hematite Is Red: Correlation of Optical Absorption Intensities and Magnetic Moments of Fe^{3+} Minerals. *Mineral Spectroscopy: A Tribute to Roger G. Burns, Special Publication*; Geochemical Society, 1996; No. 5.
(47) Bishop, J. L.; Murad, E. *Am. Mineral.* **2005**, *90* (7), 1100−1107.
(48) Drillon, M.; Panissod, P.; Rabu, P.; Souletie, J.; Ksenofontov, V.; Gütlich, P. *Phys. Rev. B: Condens. Matter Mater. Phys.* **2002**, *65* (10), 104404.
(49) Calzado, C. J.; Sanz, J. F.; Malrieu, J. P. *J. Chem. Phys.* **2000**, *112* (11), 5158−5167.
(50) Calzado, C. J.; Cabrero, J.; Malrieu, J. P.; Caballol, R. *J. Chem. Phys.* **2002**, *116* (7), 2728−2747.
(51) Zhang, F.; Rice, T. *Phys. Rev. B: Condens. Matter Mater. Phys.* **1990**, *41* (10), 7243.
(52) Zhang, F.; Rice, T. *Phys. Rev. B: Condens. Matter Mater. Phys.* **1988**, *37* (7), 3759.